

LETTER TO THE EDITOR

Nitrogen hydrides in the cold envelope of IRAS16293-2422[★]

P. Hily-Blant¹, S. Maret¹, A. Bacmann^{1,2}, S. Bottinelli⁶, B. Parise¹⁰, E. Caux⁶, A. Faure¹, E.A. Bergin²⁵, G.A. Blake³, A. Castets¹, C. Ceccarelli¹, J. Cernicharo⁹, A. Coutens⁶, N. Crimier^{1,9}, K. Demyk⁶, C. Dominik^{12,13}, M. Gerin²⁸, P. Hennebelle²⁸, T. Henning²⁶, C. Kahane¹, A. Klotz⁶, G. Melnick¹⁸, L. Paganì⁸, P. Schilke^{10,20}, C. Vastel⁶, V. Wakelam², A. Walters⁶, A. Baudry², T. Bell³, M. Benedettini⁴, A. Boogert⁵, S. Cabrit⁸, P. Caselli⁷, C. Codella¹¹, C. Comito¹⁰, P. Encrenaz⁸, E. Falgarone²⁸, A. Fuente¹⁴, P.F. Goldsmith¹⁵, F. Helmich¹⁶, E. Herbst¹⁷, T. Jacq², M. Kama¹², W. Langer¹⁵, B. Lefloch¹, D. Lis³, S. Lord⁵, A. Lorenzani¹¹, D. Neufeld¹⁹, B. Nisini²⁴, S. Pacheco¹, T. Phillips³, M. Salez⁸, P. Saraceno⁴, K. Schuster²¹, X. Tielens²², F. van der Tak^{16,27}, M.H.D. van der Wiel^{16,27}, S. Viti²³, F. Wyrowski¹⁰, and H. Yorke¹⁵

(Affiliations can be found after the references)

Preprint online version: January 19, 2014

ABSTRACT

Nitrogen is the fifth most abundant element in the Universe, yet the gas-phase chemistry of N-bearing species remains poorly understood. Nitrogen hydrides are key molecules of nitrogen chemistry. Their abundance ratios place strong constraints on the production pathways and reaction rates of nitrogen-bearing molecules. We observed the class 0 protostar IRAS16293-2422 with the heterodyne instrument HIFI, covering most of the frequency range from 0.48 to 1.78 THz at high spectral resolution. The hyperfine structure of the amidogen radical o-NH₂ is resolved and seen in absorption against the continuum of the protostar. Several transitions of ammonia from 1.2 to 1.8 THz are also seen in absorption. These lines trace the low-density envelope of the protostar. Column densities and abundances are estimated for each hydride. We find that NH:NH₂:NH₃ ≈ 5:1:300. Dark clouds chemical models predict steady-state abundances of NH₂ and NH₃ in reasonable agreement with the present observations, whilst that of NH is underpredicted by more than one order of magnitude, even using updated kinetic rates. Additional modelling of the nitrogen gas-phase chemistry in dark-cloud conditions is necessary before having recourse to heterogen processes.

Key words. ISM: abundances, Astrochemistry, ISM individual objects: IRAS 16293-2422

1. Introduction

Nitrogen is the fifth most abundant element in the Universe and is a fundamental component of molecules associated with life. Nitrogen-bearing molecules are routinely observed towards a wide variety of environments, from the diffuse interstellar medium (Liszt & Lucas 2001) to pre-stellar cores (Bergin & Tafalla 2007) and protoplanetary disks (Dutrey et al. 1997). Complex N-bearing molecules are also observed towards star-forming regions (Herbst & van Dishoeck 2009). The chemical network of nitrogen is apparently simple in that a small set of reactions is involved (Pineau des Forêts et al. 1990, hereafter PdF90). The chemistry of nitrogen has been modelled in various environments with moderate success, including typical dark cloud conditions (Millar et al. 1991; Le Bourlot 1991), shocks (PdF90), pre-stellar cores (Flower et al. 2006; Maret et al. 2006; Hily-Blant et al. 2010), and photo-dissociation regions (PDR) (Sternberg & Dalgarno 1995). One major unknown is the total abundance, in dense and shielded environments, of gas-phase nitrogen, the reservoir of which consist of N and/or N₂. Because they are not directly observable, estimates of their abundances rely on observations of other N-bearing compounds and chemical modelling. Observational constraints of the dominant chemical pathways of the nitrogen chemistry and their kinetic rates are thus crucial.

In this respect, nitrogen hydrides are of utmost importance since they are among the first neutral N-bearing molecules formed in an initially atomic gas dominated by hydrogen and helium. Ammonia was among the first interstellar molecules detected in emission towards the Galactic centre (Cheung et al. 1968). The lightest radical, imidogen NH, was observed in absorption by Meyer & Roth (1991) along the diffuse line of sight towards ζPer. Gas-phase models were found to underestimate the abundance of NH, and dust grains were then proposed to solve part of the discrepancy (Meyer & Roth 1991; Wagenblast et al. 1993). Amidogen (NH₂) was observed in absorption by van Dishoeck et al. (1993) from dense gas in Sgr B2. This source was also targeted by Goicoechea et al. (2004) with ISO. The ratios of the three hydrides were found to be NH:NH₂:NH₃ ≈ 1:10:100, incompatible with the dark cloud value NH₃/NH₂ < 3 predicted by Millar et al. (1991). Unfortunately, the modelling of the chemistry in Sgr B2 is difficult due to the complexity of the source, which probably incorporates shock dynamics. The NH:NH₂:NH₃ ratios measured in Sgr B2 may thus not be representative of cold dark clouds, and the chemistry of nitrogen hydrides in these environments remains largely unexplored.

In this paper, we present HIFI observations of the submillimetre lines of NH₂ and NH₃ in absorption against the continuum of the class 0 protostar IRAS16293-2422. Section 2 summarizes the observation strategy and data reduction. In Sect. 3 we derive the column densities of NH₂ and NH₃. Abundances of

[★] Herschel is an ESA space observatory with science instruments provided by European-led principal Investigator consortia and with important participation from NASA.

the three lightest nitrogen hydrides are estimated in Sect. 4, and compared to steady-state models using updated reaction rates.

2. Observations and data reduction

The solar-mass protostar IRAS16293-2422 was observed with the HIFI instrument onboard the Herschel Space Observatory, as part of the HIFI guaranteed time key program CHES (Ceccarelli et al. 2010). Full spectral coverage of bands 1a (480 – 560 GHz), 3b (858 – 961 GHz), 4a (949 – 1061 GHz), 5a (1.12 – 1.24 THz), and 7a (1.70 – 1.79 THz) were performed on 2010 Mar 1, 3, and 19, using the Spectral Scan DSB mode with optimization of the continuum. The Wide Band Spectrometre (WBS) was used as a backend, providing us with a spectral resolution of 1.1 MHz over an instantaneous bandwidth of 4×1 GHz. The targeted coordinates were $\alpha_{2000} = 16^h 32^m 22^s.75$, $\delta_{2000} = -24^\circ 28' 34.2''$. The two reference positions were situated approximately $3'$ east and west of the source. The beam size is well approximated by $HPBW = 21.5''/\nu_{\text{THz}}$. For the analysis, intensities were then brought to a main-beam temperature scale using $F_{\text{eff}} = 0.96$ and $B_{\text{eff}} = 0.70$.

The data were processed using the standard HIFI pipeline HIPE 2.8 (Ott 2010) up to frequency and amplitude calibrations (level 2). For the SIS bands 1 to 5, a single local-oscillator-tuning spectrum consists of 4 sub-bands of 1 GHz for each polarization. The 1 GHz chunks for bands 1 to 5 are then exported as FITS files in the CLASS90/GILDAS format¹ (Hily-Blant et al. 2005) for subsequent data reduction and analysis. Despurring and residual bandpass effect subtraction were performed in CLASS90 using generic spectral-survey tools developed in our group. Sideband deconvolution is computed with the minimization algorithm of Comito & Schilke (2002) implemented into CLASS90. Line identification used the Weeds CLASS90-add-on developed by Maret et al. (2010), which provides an efficient interface to the public CDMS and JPL spectroscopic databases (Müller et al. 2001; Pickett et al. 1998).

3. Results

Figure 1 shows the detection of the hyperfine structure (HFS) of the $N = 0 - 1$, $J = \frac{1}{2} - \frac{3}{2}$, and $J = \frac{1}{2} - \frac{1}{2}$ transitions of amidogen in its ortho form, with their strongest components at the rest frequencies 952.578354 GHz and 959.511716 GHz, respectively (Müller et al. 1999). The HFS is almost entirely resolved with an intensity ratio that clearly deviates from optically thin LTE excitation. The 3σ noise levels are indicated in each panel. The para- NH_2 line was not detected and a 5σ upper limit to the main HFS component at 947.725 GHz is $\int \tau dv \leq 0.2 \text{ km s}^{-1}$. Figure 2 shows several transitions of ammonia seen in absorption, from 1168.4 to 1763.8 GHz. The fundamental rotational transition at 572.6 GHz was also detected in emission (see Fig. A.3) but because it contains both emission and absorption, it is not discussed in this paper.

All column densities are derived assuming a single excitation temperature T_{ex} for each molecule. The opacity of each HFS component and the excitation temperature are determined by simultaneously fitting all HFS components, constraining the opacities to scale with $A_{ul}g_u$. The fit is performed in CLASS90 by applying the HFS method to the continuum-subtracted spectra $T_{\text{mb}} = [J_\nu(T_{\text{ex}}) - J_\nu(T_{\text{CMB}}) - T_C](1 - e^{-\tau_{ul}})$. The total column density reads $N_{\text{tot}} = (8\pi\nu^3/c^3) Q/(A_{ul}g_u) \times \int \tau_{ul} dv \times e^{E_{l1}/kT_{\text{ex}}}/[1 -$

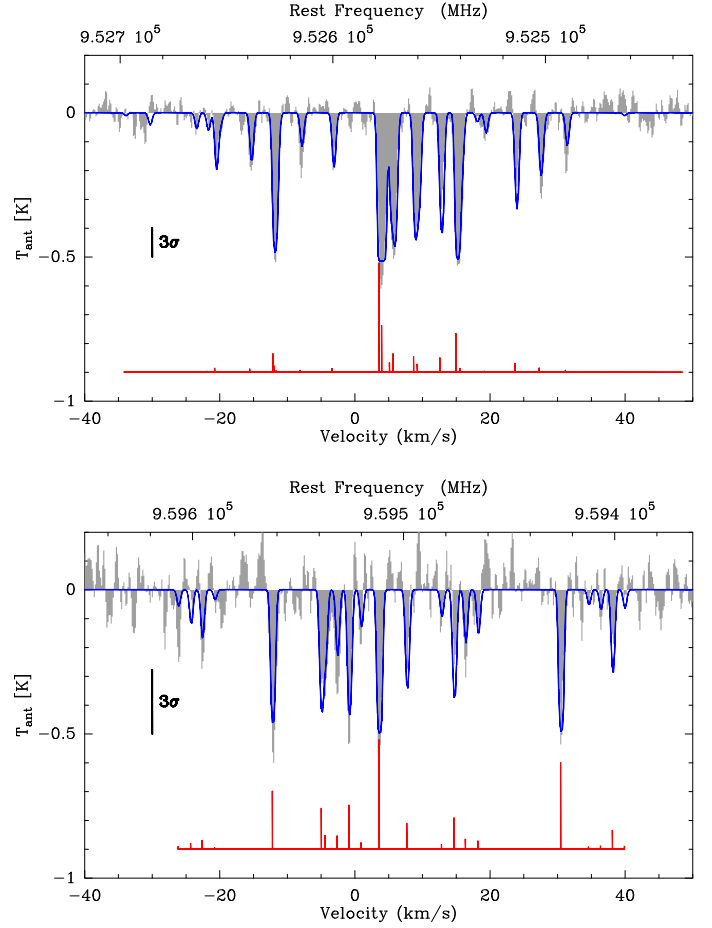


Fig. 1. Absorption spectra of o- NH_2 at 952 GHz and 959 GHz, with the HFS fit overlaid (line). The relative intensities in the optically thin LTE limit are indicated at the bottom.

$e^{-h\nu/kT_{\text{ex}}}$, where Q is the partition function at T_{ex} . In deriving the excitation temperature, we assumed equal filling factors for the absorbing gas and the background continuum radiation. The SSB continuum intensity T_C , needed to derive T_{ex} ,

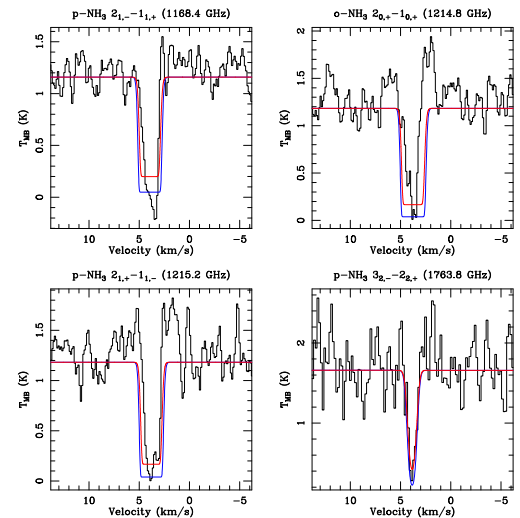


Fig. 2. NH_3 absorption lines from 1.168 to 1.764 THz. LTE predictions are shown in red ($T_{\text{ex}} = 10 \text{ K}$, $N(\text{NH}_3) = 3.5 \times 10^{15} \text{ cm}^{-2}$) and blue ($T_{\text{ex}} = 8 \text{ K}$, $N(\text{NH}_3) = 2 \times 10^{16} \text{ cm}^{-2}$).

¹ <http://www.iram.fr/IRAMFR/GILDAS>

Table 1. Column densities of nitrogen hydrides towards IRAS16293-2422.

Species	Transition	Component ^a	Frequency GHz	HPBW arcsec	$T_{C,mb}$ ^b K	T_I ^c K	τ_{ul}	T_{ex} K	$FWHM$ ^d km s ⁻¹	N_{tot} 10 ¹⁴ cm ⁻²
NH ^e	0 ₁ → 1 ₀	$\frac{3}{2}, \frac{3}{2} \rightarrow \frac{1}{2}, \frac{3}{2}$	946.476	23	0.8	-3.8 ± 0.6	2.8 ± 0.7	9.5	0.60	2.20 ± 0.80
o-NH ₂	0 _{00½} → 1 _{11½}	$\frac{3}{2}, \frac{3}{2} \rightarrow \frac{1}{2}, \frac{3}{2}$	952.578	23	0.9	-9.0 ± 0.5	12.8 ± 0.7	8.5	0.60	0.40 ± 0.06
	0 _{00½} → 1 _{11½}	$\frac{3}{2}, \frac{5}{2} \rightarrow \frac{3}{2}, \frac{5}{2}$	959.512	22	0.9	-2.5 ± 0.2	4.9 ± 0.7	9.5	0.60	0.59 ± 0.12
p-NH ₃	1 – 2	(1, -) – (1, -)	1168.453	18	1.2		300 – 70	8 – 10	0.50	200 – 35
o-NH ₃	1 – 2	(0, +) – (0, +)	1214.853	18	1.3		470 – 130	8 – 10	0.50	200 – 35
p-NH ₃	1 – 2	(1, +) – (1, +)	1215.246	18	1.3		330 – 80	8 – 10	0.50	200 – 35
p-NH ₃	2 – 3	(2, -) – (2, -)	1763.823	12	2.2		2.0 – 1.4	8 – 10	0.50	200 – 35

Notes. ^(a) For NH, the quantum numbers for the rotational transition N_J are $\mathbf{F}_1 = \mathbf{I}_H + \mathbf{J}$ and $\mathbf{F} = \mathbf{I}_N + \mathbf{F}_1$ (Klaus et al. 1997). For the $N_{K_a, K_c, J}$ rotational transition of NH₂, the quantum numbers are $\mathbf{F}_1 = \mathbf{I}_N + \mathbf{J}$ and $\mathbf{F} = \mathbf{I}_H + \mathbf{F}_1$ (Müller et al. 1999). In the case of ammonia, quantum numbers are given separately for $\mathbf{J} = \mathbf{N} + \mathbf{S}$ and (K, ϵ) , where ϵ is the symmetry index (see Maret et al. 2009). For these lines, the frequency given is that of the brightest HF component. ^(b) Single-sideband continuum in a T_{mb} scale. ^(c) $T_I = \tau_{ul}[J_\nu(T_{ex}) - J_\nu(T_{CMB}) - T_{C,mb}]$ from the HFS fit. In the case of ammonia, see Sect. 3. ^(d) A conservative uncertainty of 0.25 MHz (0.08 km s⁻¹) imposed by the HIPE 2.8 pipeline was retained. ^(e) The integrated line opacity is calculated as $\int \tau dv = 1.06 FWHM \times \tau_{ul}$. ^(d) Bacmann et al. (2010).

is estimated as half the median of each 1 GHz chunk computed in line-free spectral windows prior to deconvolution, assuming equal gains in the two sidebands (see details in Appendix A). It is found to increase with frequency and, for rest frequencies $\nu_{THz} = 0.492$ to 1.242 THz, T_C is well approximated by $T_C(T_{ant}, [K]) = 1.10 \nu_{THz} - 0.42$ (see Fig. A.1). At higher frequencies, T_C is estimated from the deconvolution tool in the HIPE software, assuming equal sideband gains.

For ammonia, the hyperfine components in each lines are not resolved out by our observations, so the column density and excitation temperature were determined by simultaneously fitting the 4 lines shown in Fig. 2. The 1763.8 GHz line has a well constrained centre-line opacity, yet the excitation temperature and column density remain degenerate. We therefore varied the excitation temperature between 5 to 15 K, and adjusted accordingly the column density until the observed line profiles were reproduced. The line width was fixed to 0.5 km s⁻¹. For $T_{ex} > 10$ K, the absorption lines at 1.11684, 1.2148, and 1.2152 THz become significantly weaker than observed. In contrast, for $T_{ex} < 8$ K, the column density needed to reproduce the 1.7 THz line becomes so large that the 1.2 THz lines broaden significantly. The full set of constraints points towards $T_{ex} \approx 8 - 10$ K and $N_{tot} \approx 2.0 \times 10^{16} - 3.5 \times 10^{15}$ cm⁻². Figure 2 shows the results of the modelled lines corresponding to $T_{ex} = 8$ and 10 K. The non-detection of the 1.7635 and 1.7636 THz absorption lines (not shown in Fig. 2) is consistent with these models.

The results are summarized in Table 1. The excitation temperature of the 952 and 959 GHz transitions of o-NH₂ are significantly higher than 2.73 K. The different values for each HFS most likely results from the LTE assumption not being entirely valid. However, $T_{ex} \ll h\nu/k$, so that the corresponding uncertainties have negligible consequences on the column density. The thermalized ortho:para ratio is expected to be large at low temperatures ($\approx e^{30.39/T}$, see Fig. A.2). Our two determinations of the o-NH₂ column density thus give an average for the total NH₂ column density. The resulting NH₂ and NH₃ column densities are $0.44 \pm 0.07 \times 10^{14}$ cm⁻² and $\approx 35 - 200 \times 10^{14}$ cm⁻², respectively. The column density ratios are thus NH/NH₂ = 5.0 ± 1.2 and NH₃/NH₂ = 90 – 500, or NH:NH₂:NH₃ ≈ 5:1:300.

4. Discussion

From Table 1, the low excitation temperatures indicate that all lines are sub-thermally excited and therefore most likely trace regions with densities much lower than their critical densities, which are of the order of 10⁷ cm⁻³. The physical source model

of Crimier et al. (2010) predicts densities lower than $\approx 10^6$ cm⁻³ for radii larger than 2400 AU or 17'' at a distance of 120 pc, comparable to the HPBW of the present observations, thus supporting the assumption of equal filling-factors for the absorbing gas and the continuum emission. At these radii, the modelled gas temperature is lower than 20 K. The NH and NH₂ linewidths are thus dominated by non-thermal broadening suggesting that turbulence has not been dissipated in the absorbing gas.

To place constraints on the average abundances in the foreground absorbing material, we need to measure the total H column density, which is not directly observable. The one-dimensional density profile of Crimier et al. (2010) is extended to lower densities as $n_{H_2}(r) = 3 \times 10^8 (r/85AU)^{-1.8} + 10^3$ cm⁻³, to allow for a low-density envelope. The column density profile, convolved by the HIFI beam, is dominated by the lines-of-sight close to the centre. Considering only the gas in the regions with $n_{H_2} < 10^6$ cm⁻³, the column density is $N(H_2) \approx 8 \times 10^{22}$ cm⁻² or 80 magnitudes of visual extinction (assuming standard dust properties and that all H is molecular). Were the hydrides absorption to occur at densities lower than 10⁴ or 10⁵ cm⁻³, the total column density would decrease by a factor 3. Therefore, in the following we estimate the abundances assuming $N(H_2) = 5.5 \pm 2.5 \times 10^{22}$ cm⁻². Results are summarized in Table 2.

The column density ratios observed in the cold envelope of IRAS16293-2422 differ from those derived by Goicoechea et al. (2004), who found NH:NH₂:NH₃=1:10:100 towards Sgr B2. These authors noted that these ratios are not consistent with typical dark cloud conditions but can be explained by shock chemistry. Though the NH₃/NH₂ ratios are similar in both the cold envelope and the Sgr B2 region, the NH/NH₂ ratios are drastically different, suggesting that different chemistry is at work in the two sources. To study this, we have employed the Astrochem gas-phase chemical code of Maret & Bergin (2010) combined with modified versions of the osu.09.2008 chemical network². Typical physical conditions for a cold molecular cloud (gas temperature $T = 10$ K, $n_H = 2 \times 10^4$ cm⁻³, $A_V = 10$ mag) and a cosmic-ray ionization rate $\zeta = 1.3 \times 10^{-17}$ s⁻¹ were used. Higher extinctions would not modify the predicted steady-state abundances. In a similar way, higher densities would shorten the time to reach a steady-state but would not alter the corresponding abundances. The initial abundances are taken from Wakelam & Herbst (2008) for which the C/O gas-phase abundance ratio is 0.41. The resulting time-dependent fractional abundances of the nitrogen hydrides are shown on Fig. B.1. The steady-state is reached after a few 10⁶ yrs, for which the

² <http://www.physics.ohio-state.edu/~eric/research.html>

Table 2. Predicted steady-state fractional abundances of several nitrogen-bearing species in three different models.

Species	I	II	III	Observations
N_2H^+ ^a	100:0	90:10	90:10	
NH_4^+ ^b	85:2:13	85:2:13	95:2:3	
N_2	1.0(-5)	1.0(-5)	1.0(-5)	–
N	2.4(-7)	2.5(-7)	2.9(-7)	–
NH	3.5(-11)	9.5(-11)	8.8(-11)	$2.0 \pm 1.0(-9)$
NH_2	1.9(-10)	1.9(-10)	1.3(-10)	$4.0 \pm 2.0(-10)$
NH_3	3.7(-8)	3.7(-8)	8.3(-8)	$0.3^{+0.1}_{-0.1} - 2^{+0.8}_{-0.8}(-8)$
$NH:NH_2:NH_3$	0.2:1:190	0.5:1:190	0.7:1:640	5:1:300

Notes. Numbers in parenthesis are powers of ten. Branching ratios (BR) for the dissociative recombination (DR) of NH_2^+ are $N + H_2$ (4%), $NH + H$ (39%) and $N + 2H$ (57%) (Thomas et al. 2005). ^(a) BR for the DR of N_2H^+ into $N_2 + H$ and $NH + N$, respectively (Molek et al. 2007; Adams et al. 2009). ^(b) BR for the DR of NH_4^+ into $NH_3 + H$, $NH_2 + H_2$, and $NH_3 + 2H$, respectively (Öjekull et al. 2004). See additional details in Table B.1.

$NH:NH_2:NH_3$ abundance ratios are 0.2:1:190 (see Table 2). We note that the $NH:NH_2:NH_3$ ratios are roughly constant for times $> 10^5$ yrs. If NH_3/NH_2 is consistent with the observations to within a factor of 2, the steady-state NH/NH_2 ratio is too small by more than one order of magnitude because the abundance of NH is underpredicted by our model.

NH_2 and NH_3 are principally formed by the dissociative recombination (DR) of NH_4^+ (Le Boulrot 1991). The formation of NH is dominated by $NH_2(O,OH)NH$, unless the NH channel of the DR of N_2H^+ has a non-zero branching ratio (BR). There are still disparate results for the BR of these DR reactions, and the most recent literature (see Table 2 and Florescu-Mitchell & Mitchell 2006) suggest uncertainties of at least 10% in the BR. We conducted three model calculations, where we varied the BR by 10%, to explore the effects on $NH:NH_2:NH_3$. The results are summarized in Table 2. The abundances vary at most by factors of a few. Noticeable is the increase in $n(NH)$ associated with the opening of the NH channel of the DR of N_2H^+ . In any case, NH remains underabundant by almost two orders of magnitude. This deficit is reminiscent of the early results obtained in the diffuse medium that motivated the recourse to surface reactions. We recall that our models do not include freeze-out onto dust grains to enhance the role of gas-phase reactions. In the case of NH formation, however, the role of surface reactions is poorly constrained.

5. Conclusions

We have presented absorption spectra of the hyperfine structure of NH_2 and several transitions of NH_3 . These lines emanate from the low density envelope of the protostar, at densities lower than typically 10^6 cm^{-3} , representative of typical dark cloud conditions. We have determined the column densities, as well as fractional abundances. We have found that $NH:NH_2:NH_3 \approx 5:1:300$. On the basis of an updated chemical network, we have computed the steady-state abundances of amidogen and ammonia, which agree well with observed values. Imidogen is underpredicted by more than one order of magnitude, and $NH/NH_2 \leq 1$. At this point, more observations (of *e.g.* ^{15}N isotopologues) and modelling are clearly needed. Freeze-out and surface reactions, not included in our calculations, are potentially important. Before having recourse to dust surface processes, however, gas-phase chemistry has to be explored in far more details in studying *e.g.*, the influence of the gas-phase C/O ratio (Hily-Blant et al. 2010) or the effects of the H_2 o:p ratio. The consequences of the uncertainties in the rates of the

dominant chemical paths (dissociative recombinations, neutral-neutral reactions at low temperature) shall also be explored in the process.

Acknowledgements. We thank the anonymous referee for useful comments. This paper benefitted from the CDMS and JPL databases. A. Faure is warmly acknowledged for his careful review of the reaction rates. HIFI has been designed and built by a consortium of institutes and university departments from across Europe, Canada and the United States under the leadership of SRON Netherlands Institute for Space Research, with major contributions from Germany, France and the US. Consortium members are: Canada: CSA, U.Waterloo; France: CESR, LAB, LERMA, IRAM; Germany: KOSMA, MPIfR, MPS; Ireland, NUI Maynooth; Italy: ASI, IFSI-INAF, Osservatorio Astrofisico di Arcetri-INAF; Netherlands: SRON, TUD; Poland: CAMK, CBK; Spain: Observatorio Astronómico Nacional (IGN), Centro de Astrobiología (CSIC-INTA). Sweden: Chalmers University of Technology - MC2, RSS & GARD; Onsala Space Observatory; Swedish National Space Board, Stockholm University - Stockholm Observatory; Switzerland: ETH Zurich, FHNW; USA: Caltech, JPL, NHSC.

References

- Adams, N. G., Herd, C. R., Geoghegan, M., Smith, D., & Canosa, A. 1991, *J. Chem. Phys.*, 94, 4852
- Adams, N. G., Molek, C. D., & McLain, J. L. 2009, *Journal of Physics Conference Series*, 192, 012004
- Bacmann, A., Caux, E., Hily-Blant, P., Parise, B., & Pagani, L. 2010, accepted to *A&A*
- Bergin, E. A. & Tafalla, M. 2007, *Annual Review of Astronomy and Astrophysics*, 45, 339
- Ceccarelli, C., Bacmann, A., Boogert, A., & CHESS team. 2010, *A&A*, this volume
- Cheung, A. C., Rank, D. M., Townes, C. H., Thornton, D. D., & Welch, W. J. 1968, *Physical Review Letters*, 21, 1701
- Comito, C. & Schilke, P. 2002, *A&A*, 395, 357
- Crimier, N., Ceccarelli, C., Maret, S., et al. 2010, *ArXiv e-prints*
- Dutrey, A., Guilloteau, S., & Bachiller, R. 1997, *A&A*, 325, 758
- Florescu-Mitchell, A. I. & Mitchell, J. B. A. 2006, *Physics Reports*, 430, 277
- Flower, D. R., Pineau des Forêts, G., & Walmsley, C. M. 2006, *A&A*, 456, 215
- Geppert, W. D., Thomas, R., Semaniak, J., et al. 2004, *ApJ*, 609, 459
- Goicoechea, J. R., Rodríguez-Fernández, N. J., & Cernicharo, J. 2004, *ApJ*, 600, 214
- Herbst, E. & van Dishoeck, E. F. 2009, *Annual Review of Astronomy and Astrophysics*, 47, 427
- Hily-Blant, P., Pety, J., & Guilloteau, S. 2005, *CLASS evolution: I. Improved OTF support*, Tech. rep., IRAM
- Hily-Blant, P., Walmsley, M., Pineau des Forêts, G., & Flower, D. 2010, *Astronomy & Astrophysics*, 513, A41+
- Klaus, T., Takano, S., & Winnewisser, G. 1997, *A&A*, 322, L1
- Le Boulrot, J. 1991, *A&A*, 242, 235
- Liszt, H. & Lucas, R. 2001, *A&A*, 370, 576
- Maret, S., Bergin, E. A., & Lada, C. J. 2006, *Nature*, 442, 425
- Maret, S. & Bergin, T. 2010, *in prep.*
- Maret, S., Faure, A., Scifoni, E., & Wiesenfeld, L. 2009, *MNRAS*, 399, 425
- Maret, S., Hily-Blant, P., Bardeau, S., Pety, J., & Reynier, E. 2010, *in prep.*
- Meyer, D. M. & Roth, K. C. 1991, *ApJ*, 376, L49
- Millar, T. J., Bennett, A., Rawlings, J. M. C., Brown, P. D., & Charnley, S. B. 1991, *A&AS*, 87, 585
- Mitchell, B. 1990, *Phys. Rep.*, 186, 215
- Molek, C. D., McLain, J. L., Poterya, V., & Adams, N. G. 2007, *J. Phys. Chem. A*, 111, 6760
- Müller, H. S. P., Klein, H., Belov, S. P., et al. 1999, *Journal of Molecular Spectroscopy*, 195, 177
- Müller, H. S. P., Thorwirth, S., Roth, D. A., & Winnewisser, G. 2001, *A&A*, 370, L49
- Öjekull, J., Andersson, P. U., NâGâRd, M. B., et al. 2004, *Journal of Chemical Physics*, 120, 7391
- Ott, S. 2010, in *Astronomical Data Analysis Software and Systems XIX*, ed. Y. Mizumoto, K.-I. Morita, & M. Ohishi (ASP Conference Series)
- Pickett, H. M., Poynter, I. R. L., Cohen, E. A., et al. 1998, *Journal of Quantitative Spectroscopy and Radiative Transfer*, 60, 883
- Pineau des Forêts, G., Roueff, E., & Flower, D. R. 1990, *MNRAS*, 244, 668
- Sternberg, A. & Dalgarno, A. 1995, *Ap. J. Supp.*, 99, 565
- Talbi, D. 2009, *Journal of Physics Conference Series*, 192, 012015
- Thomas, R. D., Hellberg, F., Neau, A., et al. 2005, *Phys. Rev. A*, 71, 032711
- van Dishoeck, E. F., Jansen, D. J., Schilke, P., & Phillips, T. G. 1993, *ApJ*, 416, L83+

Wagenblast, R., Williams, D. A., Millar, T. J., & Nejad, L. A. M. 1993, MNRAS, 260, 420
Wakelam, V. & Herbst, E. 2008, ApJ, 680, 371

-
- ¹ Laboratoire d'Astrophysique de Grenoble, UMR 5571-CNRS, Université Joseph Fourier, Grenoble, France
² Université de Bordeaux, Laboratoire d'Astrophysique de Bordeaux, CNRS/INSU, UMR 5804, Floirac, France
³ California Institute of Technology, Pasadena, USA
⁴ INAF - Istituto di Fisica dello Spazio Interplanetario, Roma, Italy
⁵ Infrared Processing and Analysis Center, Caltech, Pasadena, USA
⁶ Centre d'Etude Spatiale des Rayonnements, Université Paul Sabatier, Toulouse 3, CNRS UMR 5187, Toulouse, France
⁷ School of Physics and Astronomy, University of Leeds, Leeds UK
⁸ LERMA and UMR 8112 du CNRS, Observatoire de Paris, 61 Av. de l'Observatoire, 75014 Paris, France
⁹ Centro de Astrobiología, CSIC-INTA, Madrid, Spain
¹⁰ Max-Planck-Institut für Radioastronomie, Bonn, Germany
¹¹ INAF Osservatorio Astrofisico di Arcetri, Florence Italy
¹² Astronomical Institute 'Anton Pannekoek', University of Amsterdam, Amsterdam, The Netherlands
¹³ Department of Astrophysics/IMAPP, Radboud University Nijmegen, Nijmegen, The Netherlands
¹⁴ IGN Observatorio Astronómico Nacional, Alcalá de Henares, Spain
¹⁵ Jet Propulsion Laboratory, Caltech, Pasadena, CA 91109, USA
¹⁶ SRON Netherlands Institute for Space Research, Groningen, The Netherlands
¹⁷ Ohio State University, Columbus, OH, USA
¹⁸ Harvard-Smithsonian Center for Astrophysics, Cambridge MA, USA
¹⁹ Johns Hopkins University, Baltimore MD, USA
²⁰ Physikalisches Institut, Universität zu Köln, Köln, Germany
²¹ Institut de RadioAstronomie Millimétrique, Grenoble - France
²² Leiden Observatory, Leiden University, Leiden, The Netherlands
²³ Department of Physics and Astronomy, University College London, London, UK
²⁴ INAF - Osservatorio Astronomico di Roma, Monte Porzio Catone, Italy
²⁵ Department of Astronomy, University of Michigan, Ann Arbor, USA
²⁶ Max-Planck-Institut für Astronomie, Heidelberg, Germany
²⁷ Kapteyn Astronomical Institute, University of Groningen, The Netherlands
²⁸ LERMA, UMR 8112-CNRS, Ecole Normale Supérieure et Observatoire de Paris, France

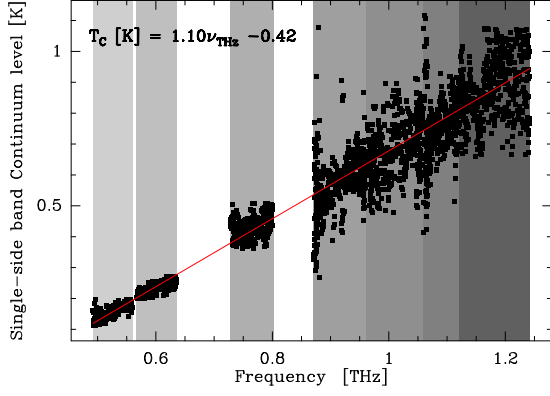


Fig. A.1. Double sideband continuum (in antenna temperature scale) level towards IRAS16293-2422, from 0.5 to 1.2 THz. The straight line is the result of a linear fit. The observed HIFI bands are highlighted.

Appendix A: Determination of the column density

Figure A.1 displays the double-sideband continuum intensity measured from 0.5 to 1.2 THz with the double-sideband receivers of the HIFI instrument. The single-sideband continuum is then estimated assuming equal image and signal gains. The SSB continuum intensity was estimated following two independent methods. First, the median of the intensity in each 1 GHz sub-band was computed. The resulting double-sideband (DSB) continuum level T_C , sampled every 0.25 GHz from 0.492 THz to 1.242 THz, was found to increase linearly with the frequency (see Fig. A.1). The second method consisted in deconvolving the despoiled spectra prior to baseline subtraction, the result of which is the SSB continuum level. The DSB deconvolution was applied to the subset of spectra covering the spectral ranges of the lines considered in this paper. The DSB continuum level is twice the SSB to better than 10% in these intervals. From the first method, the antenna temperature scale SSB continuum level is well fitted by a 1st order polynomial as $T_C[\text{K}] = 1.10 \nu_{\text{THz}} - 0.42$, for rest frequencies ν_{THz} ranging from 0.492 to 1.242 THz (see Fig. A.1). The increase in T_C with frequency might be caused by the convolution of the dust temperature profile with the telescope beam. It may also trace the increase in the dust emissivity with frequency. At the higher frequencies of the ammonia lines in Band 7, the continuum level was estimated using the second method, in HIPE.

Figure A.2 shows the o:p ratio for NH_2 assuming equilibrium at a single temperature for all levels.

Appendix B: Chemical modelling

Nitrogen chemistry starts with the formation of NO and CN by means of the reactions $\text{N}(\text{OH}, \text{NO})\text{H}$ and $\text{N}(\text{CH}, \text{H})\text{CN}$, which then lead to N_2 (Hily-Blant et al. 2010). Once N_2 is formed, it reacts with He^+ to form N^+ , which, by successive hydrogen abstractions, leads quickly to NH^+ , NH_2^+ , NH_3^+ , and NH_4^+ . The dissociative recombination (DR) of NH_4^+ is the dominant formation route for NH_2 and NH_3 . The formation of NH is dominated by $\text{NH}_2(\text{O}, \text{H})\text{NH}$, unless the NH channel of the DR of N_2H^+ has a non-zero branching ratio (BR). Although DR branching ratios have been (re)measured recently for N_2H^+ , NH_2^+ , and NH_4^+ , there are still disparate results and significant uncertainties. According to the most recent literature (see Table 2 and Florescu-Mitchell & Mitchell 2006), the BR of DR reactions are

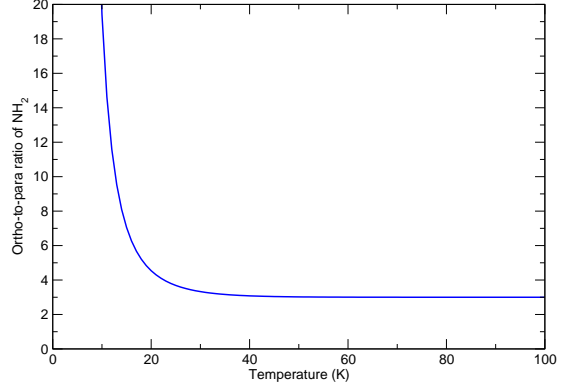


Fig. A.2. Thermalized ortho:para ratio for NH_2 .

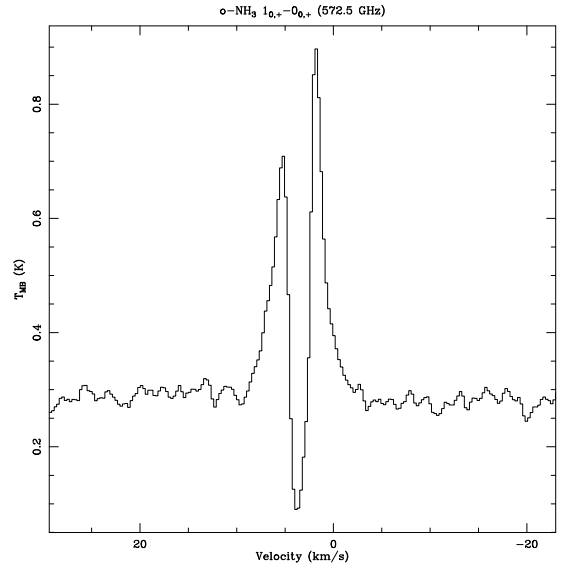


Fig. A.3. Emission line of the fundamental transition of NH_3 at 572.6 GHz detected by HIFI towards IRAS16293-2422.

uncertain by at least 10%. We conducted three model calculations, where we varied the BR by 10%, to explore the effects on $\text{NH}:\text{NH}_2:\text{NH}_3$. The results are summarized in Table 2. The abundances vary at most by factors of a few. We note the increase in $n(\text{NH})$, which is associated with the opening of the NH channel of the DR of N_2H^+ . In any case, NH remains underabundant by almost two orders of magnitude. This deficit is reminiscent of the early results obtained in the diffuse medium that motivated the recourse to surface reactions. We recall that our models do not include freeze-out onto dust grains to ensure that the role of gas-phase reactions is enhanced. In the case of NH formation, however, the role of surface reactions is largely ill-constrained.

To model the steady-state abundances of the nitrogen hydrides, the *osu.09.2008* network and rates were used. The *osu.09.2008* network contains 13 elements, 449 species, and 4457 gas-phase reactions. We note that this version of the OSU database does not contain molecular anions or any depletion of gas-phase species. The network has been updated from a revision of the branching ratios and rate coefficients for the dissociative recombination (DR) of the nitrogen bearing cations N_2H^+ , NH_2^+ , and NH_4^+ :

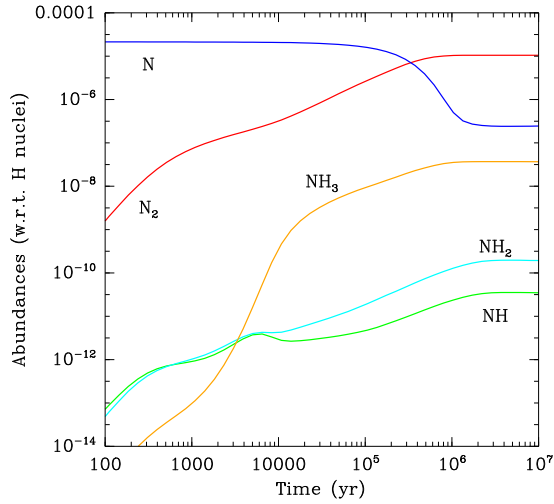


Fig. B.1. Predicted abundances for several N-bearing molecules as a function of time for model 1 (“standard”, see text), for a density $n_{\text{H}} = 2 \times 10^4 \text{ cm}^{-3}$, a gas temperature $T_{\text{kin}} = 10 \text{ K}$, and a total extinction $A_{\text{V}} = 10 \text{ mag}$. Abundances are given with respect to H nuclei.

- The DR of N_2H^+ has been determined experimentally using both flowing afterglow (FA, see Adams et al. 1991) and storage ring (SR) techniques (Geppert et al. 2004), leading to controversial results concerning the branching ratios (BR) of the two channels $\text{N}_2 + \text{H}$ and $\text{NH} + \text{N}$. Thus, in contrast to the FA results that established the major product as $\text{N}_2 + \text{H}$ with a BR $\approx 100\%$, Geppert et al. (2004) found this channel to account for only 36% of the total reaction. The most recent FA and SR measurements (Molek et al. 2007; Adams et al. 2009), however, have confirmed the earlier FA results that the DR of N_2H^+ should lead predominantly to $\text{N}_2 + \text{H}$ with a BR $\approx 90 - 100\%$. This result is also supported by the *ab initio* calculations of Talbi (2009). For the total rate coefficient, we adopted the (temperature dependent) expression of Geppert et al. (2004), as in the `osu.09.2008` network.
- For the DR of NH_2^+ , the latest SR measurements are those of Thomas et al. (2005), who obtained the BR for $\text{N} + \text{H}_2$ (4%), $\text{NH} + \text{H}$ (39%), and $\text{N} + 2\text{H}$ (57%). For the rate coefficient, we adopted the expression recommended by Mitchell (1990), as in the `osu.09.2008` network.
- Finally, the SR measurements of Öjekull et al. (2004) demonstrated that the DR of NH_4^+ is dominated by the product channels $\text{NH}_3 + \text{H}$ (85%), $\text{NH}_2 + 2\text{H}$ (13%), and $\text{NH}_2 + \text{H}_2$ (2%). For the total rate, we adopted the expression of Öjekull et al. (2004), which differs slightly from the one recommended in the `osu.09.2008` network.

We note that for NH_3^+ there is to our knowledge neither measurements nor calculations available. We therefore adopted the rate and branching ratios recommended in the `osu.09.2008` network, corresponding to the two channels $\text{NH} + 2\text{H}$ (50%) and $\text{NH}_2 + \text{H}$ (50%).

Following the above update of DR rates and branching ratios, we have adopted three different chemical models by varying the DR branching ratios of N_2H^+ and NH_4^+ within 10%, the typical experimental uncertainty. The DR of these two ions was indeed found to be the dominant formation routes of NH and NH_2 , respectively. The employed branching ratios are listed in Table B.1.

Table B.1. Dissociative recombination branching ratios employed in the present work.

Ion	Total rate ^d		Products	Model		
	γ	β		1	2	3
N_2H^{+b}	1.00(-7)	-0.5	$\text{N}_2 + \text{H}$	100%	90%	90%
			$\text{NH} + \text{H}$	0%	10%	10%
NH_2^{+c}	3.00(-7)	-0.5	$\text{N} + \text{H} + \text{H}$	57%		
			$\text{N} + \text{H}_2$	4%		
			$\text{NH} + \text{H}$	39%		
NH_3^+	3.10(-7)	-0.5	$\text{NH} + \text{H} + \text{H}$	50%		
			$\text{NH}_2 + \text{H}$	50%		
NH_4^{+d}	9.40(-7)	-0.6	$\text{NH}_3 + \text{H}$	85%	85%	95%
			$\text{NH}_2 + \text{H}_2$	2%	2%	2%
			$\text{NH}_2 + \text{H} + \text{H}$	13%	13%	3%

Notes. ^(a) Reaction rates are written as $k = \gamma(T/300)^\beta$ in cm^3s^{-1} . ^(b) Molek et al. (2007) ^(c) Thomas et al. (2005) ^(d) Öjekull et al. (2004).